

Development of a deep machine learning interatomic potential for metalloid-containing Pd-Si compounds

Tongqi Wen^{1,2}, Cai-Zhuang Wang^{2,3,*}, M. J. Kramer², Yang Sun², Beilin Ye⁴, Haidi Wang², Xueyuan Liu²,
Chao Zhang^{2,5}, Feng Zhang², Kai-Ming Ho^{2,3}, and Nan Wang^{1,†}

¹MOE Key Laboratory of Materials Physics and Chemistry under Extraordinary Conditions, School of Natural and Applied Sciences, Northwestern Polytechnical University, Xi'an 710072, China

²Ames Laboratory-USDOE, Iowa State University, Ames, Iowa 50011, USA

³Department of Physics and Astronomy, Iowa State University, Ames, Iowa 50011, USA

⁴School of Materials Science and Engineering, South China University of Technology, Guangzhou 510641, China

⁵Department of Physics, School of Opto-electronic Information Science and Technology, Yantai University, Yantai, 264005, China



(Received 16 July 2019; revised manuscript received 8 October 2019; published 4 November 2019)

Interatomic potentials based on neural-network machine learning (ML) approach to address the long-standing challenge of accuracy versus efficiency in molecular-dynamics simulations have recently attracted a great deal of interest. Here, utilizing Pd-Si system as a prototype, we extend the development of neural-network ML potentials to compounds exhibiting various types of bonding characteristics. The ML potential is trained by fitting to the energies and forces of both liquid and crystal structures first-principles calculations based on density-functional theory (DFT). We show that the generated ML potential captures the structural features and motifs in Pd₈₂Si₁₈ and Pd₇₅Si₂₅ liquids more accurately than the existing interatomic potential based on embedded-atom method (EAM). The ML potential also describes the solid-liquid interface of these systems very well. Moreover, while the existing EAM potential fails to describe the relative energies of various crystalline structures and predict wrong ground-state structures at Pd₃Si and Pd₉Si₂ composition, the developed ML potential predicts correctly the ground-state structures from genetic algorithm search. The efficient ML potential with DFT accuracy from our study will provide a promising scheme for accurate atomistic simulations of structures and dynamics of complex Pd-Si system.

DOI: [10.1103/PhysRevB.100.174101](https://doi.org/10.1103/PhysRevB.100.174101)

I. INTRODUCTION

Molecular-dynamics (MD) simulation has been attracting growing attention in materials science, condensed-matter physics, chemical and biological science due to its ability to reveal atomic-level structures and dynamics as well as structure-property relationship [1,2]. However, to perform reliable MD simulations, accurate and efficient description of interatomic forces are critical. Quantum-mechanics calculation based on first-principles density-functional theory (DFT) can provide accurate description of interatomic forces and total energies for many materials, and *ab initio* MD (AIMD) simulations based on DFT have been applied extensively to investigate the structures and dynamics in different systems [3,4]. However, due to the expensive computational demand, AIMD can usually be performed with smaller size (~500 atoms) and shorter time (typically less than 1 ns) even with the advent of the newest-generation supercomputers. To overcome this limitation, various empirical interatomic potential schemes for MD simulations have been proposed. Traditionally, interatomic potentials are defined by assuming an analytical function with respect to the atomic

coordinates based on one's chemical and physical insights, such as Lennard-Jones potentials for noble gas and colloidal systems [5,6], Tersoff and Stillinger-Weber potentials [7,8] for covalent systems, and embedded-atom method (EAM) potentials [9] for the metallic systems. Although these potentials have been widely used in MD simulations and have produced many useful results for better understanding the structures and properties of many compounds [10,11], limitations for their application in more complex systems have also been noticed. The fixed mathematical function for the interatomic interactions inspired by human chemical and physical insights often cannot provide the balance between diverse properties stemming from different bonding characteristics [12]. New types of potential that can adapt to various bonding environments in the same systems are needed for systems with complex bonding characteristics.

Machine learning (ML) is well-known for its ability in performing pattern recognition [13]. Since the energy and forces on an atom in a condensed-matter system are predominately dependent on the species of the atom, its valence state, and interactions with its neighbors, interatomic potentials fitting can be regarded as pattern recognition problem and ML is a promising approach. Under this premise, neural-network potentials (NNPs) were first proposed by Behler and Parrinello [14] and were applied in MD simulations for systems containing thousands of atoms. In this approach, radial and

*wangcz@ameslab.gov

†nan.wang@nwpu.edu.cn

angular symmetry functions were proposed as the “descriptors” of the bonding environments to map the atomic coordinates onto the input values of the neural network. The parameters of the feed-forward neural network were then optimized by fitting to the total energies of the system. Based on the Behler-Parrinello approach to construct the NNP, the related research has expanded into a number of different systems, such as bulk silicon [14] and carbon [15], TiO₂ [16], CaF₂ [17], *et al.* However, the fixed symmetry functions reduce the flexibility of the NNPs to describe the complex bonding situations, particularly for systems with many chemical elements. Recently, Zhang *et al.* proposed a more robust and flexible method for the description of the bonding environment and developed a Deep Potential Molecular Dynamics (DEEPM) scheme based on the ML neural network to overcome this problem [18–21]. The DEEPM-KIT package has been applied successfully in various systems such as molecules, MoS₂, Pt, TiO₂, CoCrFeMnNi high-entropy alloy, Al-Mg alloy system, etc. [18–21]. We would like to note that in addition to the NNP mentioned above, development of interatomic potentials based on ML has attracted considerable research interest in recent years. For example, Schütt *et al.* [22,23] have developed a SCHNET package with the neural-network architecture and SCHNETPACK framework to accurately predict chemical properties and potential-energy surfaces of molecules. Kondor and co-workers [24] proposed a covariant composition networks framework for learning the properties of molecules from their molecular graphs and the framework can extract multiscale structure and keep track of the local topology. Furthermore, other forms of ML potentials were also proposed such as the Gaussian approximation potential [25–27], the Spectral Neighbor Analysis Potential [28–30], and the moment tensor potentials [31–33]. For all the ML potentials, the total energy is calculated as a sum of the atomic energies which are determined by the atomic configurations and various “descriptors” have been used in different types of ML potentials to depict the atomic environment. A comprehensive comparison between different ML potentials can also be found in a recent paper by Zuo *et al.* [34].

In this paper, we adopted the DEEPM-KIT to develop a NNP for Pd-Si compound as a prototype system. The motivations for choosing such a system are as follows: (i) The composition of Pd₈₂Si₁₈ can be readily fabricated into bulk metallic glasses [35] and an accurate potential at this composition can aid in understanding the metallic glass; (ii) There are many complex phases which form around the Pd₈₂Si₁₈ composition [36], and an accurate and efficient interatomic potential would be useful for determining the energy landscape and the structures of metastable phases around this composition; (iii) Solidification processes can be investigated more efficiently by employing the newly generated NNP; (iv) Since interatomic potential for this system based on EAM is available in the literature [37], the developed ML potential can be directly compared with the existing EAM potential. We will show that the generated NNP describes the structures of Pd₈₂Si₁₈ and Pd₇₅Si₂₅ liquids more accurately than the existing EAM potential. The NNP also outperforms the EAM potential in predicting the ground-state crystalline structures of Pd₃Si and Pd₉Si₂ compounds. We note that the generated NNP should be accurate for MD simulations for Pd-Si systems

with Si composition less than 25 at % where many interesting and complex new phases may exist.

The paper is organized as follows. In Sec. II, we first introduce the ML potential development process including the datasets utilized and the detailed parameters used in the DEEPM-KIT. The training and testing accuracies in comparison with the first-principles DFT results are then discussed. In Sec. III, the liquid structure obtained by NNP-MD is compared with that by AIMD and the EAM potential from Sheng [37] through the pair-distribution functions (PDFs) and the cluster alignment method [38,39]. Genetic algorithm (GA) search is used to demonstrate the promising applications of NNP in crystal-structure prediction [40,41] and the profiles and migration of the solid-liquid interface (SLI) as well as the glass-transition process from the NNP-MD simulations are also discussed in Sec. III. Finally, a brief summary is given in Sec. IV.

II. COMPUTATIONAL METHODS

A. Datasets for machine learning training and validation

Liquid datasets for the development of the NNP for Pd-Si system are generated by AIMD simulations. The AIMD simulations for Pd₈₂Si₁₈ and Pd₇₅Si₂₅ liquids and undercooled liquids are performed using 200 atoms by Vienna *Ab initio* Simulation Package (VASP) [3,42]. Projected-augmented waves with the Perdew-Burke-Ernzerhof (PBE) form of exchange-correlation potentials are adopted [43,44]. The PBE-DFT method is accurate for depicting the atomic interaction in Pd-Si system which has been validated in Refs. [45,46]. Only the Γ point is utilized to sample the Brillouin zone and the default energy cutoffs of 251 eV are employed. The AIMD simulations are carried out using the canonical ensemble (NVT) with Nosé-Hoover thermostat under periodic boundary conditions. The simulation temperatures of the two compositions are 1800, 1600, 1400, 1200, 1100, 1000, 900, and 800 K, respectively, and the liquid at lower temperatures is quenched from 1800 K at a constant cooling rate of 0.1 K/step. At each temperature, the simulation box size is adjusted to ensure that the average pressure of the system is in the range of 0.0 ± 1.0 kBar. The time step of the AIMD simulations is 3 fs and a total simulation time of 30 ps is performed at each temperature. The snapshots are recorded every 0.3 ps at each temperature and then the static DFT calculations on the AIMD structures are performed with the energy cutoff of 400 eV, k -mesh grid of $2\pi \times 1/25 \text{ \AA}^{-1}$, and the electronic convergence criterion of 10^{-5} eV in VASP. Thus, 800 frames of data consisting of total energy and the forces on each atom have been collected for each composition. In the NNP development process, 100 frames of data for each composition at 800 K are used as validating data and the remaining data are used as training data. We use the data at lower temperature of 800 K as validating data to make sure that the NNP trained by the configurations at higher temperatures can predict the atomic motion and trajectories at lower temperatures.

Besides the liquid data described above, perfect and distorted crystal structures at Pd₉Si₂ and Pd₃Si, whose compositions are close to the liquid compositions of Pd₈₂Si₁₈ and Pd₇₅Si₂₅, respectively, are also added to the training

and validating datasets. The distorted crystal structures are constructed as follows: (i) The unit cell of the perfect crystal is compressed and dilated uniformly by $\sigma_c = 0.9 + 0.01n$ ($n = 0, 1, 2, \dots, 10$) to cover various box sizes; (ii) The atomic positions in the unit cell are randomly displaced with $\sigma_a = -0.025 + 0.005n$ ($n = 0, 1, 2, \dots, 10$) times the length of the cell vector, which acts as an analogy to include the effect of thermal vibrations. In total, 1000 structures including the perfect crystal structure are generated at each composition and the energies and forces are calculated by VASP. In these calculations, plane-wave basis with the energy cutoff of 400 eV is used and the calculations are performed with a k -mesh grid of $2p \times 1/25 \text{ \AA}^{-1}$ in VASP. The electronic energy convergence criterion is 10^{-5} eV. It should be noted that these settings in VASP are the same as that of the aforementioned static calculations on AIMD structures. The 1000 configurations contain the information of atomic positions, total energies, and forces on every single atom at each composition, in which 800 configurations are used as training data and the rest are used as validating data. Furthermore, AIMD at 300 K for Pd_3Si (128 atoms) and Pd_9Si_2 (352 atoms) crystalline phases are performed followed by static calculations with the same settings as above in VASP. The total energy, atomic forces, and PDFs of the crystalline structures at 300 K for the two compositions are used to validate the generated NNP.

Combining the liquid and crystal datasets at different compositions, we have 3000 configurations in the training process and 800 configurations for the validating purpose.

B. DEEPMMD training

The DeepPot-SE model [19] in the DEEPMMD-KIT package is applied in the training process. The cutoff radius of the model is set to 6.0 Å and descriptors decay smoothly from 5.8 Å to the cutoff radius of 6.0 Å. The size of the filter and fitting networks are {50,100} and {240,240,240}, respectively. A skip connection is built (ResNet) between two neighboring fitting layers. The model is trained by the Adam stochastic gradient descent method [47] and the learning rate decreases exponentially with respect to the starting value of 0.001. The decay rate and decay step are set to 0.96 and 10 000, respectively. In addition, the prefactors in the loss functions are $p_e^{\text{start}} = 0.2$, $p_e^{\text{limit}} = 2$, $p_f^{\text{start}} = 100$, $p_f^{\text{limit}} = 1$, $p_v^{\text{start}} = 0$, $p_v^{\text{limit}} = 0$. No virial data are included in the training process.

C. MD simulations and structural analysis

With the interface of the DEEPMMD-KIT to the LAMMPS code [48], MD simulations can be directly performed with the generated NNP. To compare the liquid structures obtained by AIMD, NNP, and EAM potential, the same simulation condition is applied. Specifically, the same starting configuration, same time step (3 fs), same simulation time (30 ps), and NVT ensemble are used in AIMD and the classical MD simulations with NNP and EAM potential. Atomic coordinates are collected every 0.3 ps and in total 100 snapshots are used for further structural analysis. The total and partial PDFs of the liquid structures are compared. Furthermore, the cluster alignment method which has been used extensively in different systems [49–51] is employed to classify the atomic-

level motif. For the cluster alignment method, the alignment score is calculated as follows:

$$f = \min_{0.80 \leq \alpha \leq 1.2} \left(\frac{1}{N} \sum_{i=1}^N \frac{(\vec{r}_{ic} - \alpha \vec{r}_{it})^2}{(\alpha \vec{r}_{it})^2} \right)^{1/2}, \quad (1)$$

where N is the number of neighbor atoms in the template; \vec{r}_{ic} and \vec{r}_{it} are the atomic positions in the aligned cluster and template, respectively; and α is a coefficient to adapt the bond length of the template which is chosen to be in the range of 0.8 to 1.2 in the present study. Common motifs like body-centered cubic (bcc), fcc, hcp, and icosahedra (ICO) are used as templates in the cluster alignment process as well as the recently excavated Pd-centered 1551 (Z13) and Si-centered Z9 motifs [52]. The alignment score indicates the deviations of the cluster from the template and the smaller alignment score suggests the higher similarity between the cluster and template and vice versa.

For the MD simulations on the glass-transition process of $\text{Pd}_{82}\text{Si}_{28}$ and $\text{Pd}_{75}\text{Si}_{25}$, the isothermal-isobaric ensemble (NPT , $N = 5000$ atoms, $P = 0$) and a Nosé-Hoover thermostat are used. The periodic boundary conditions are applied in the three directions and the time step of the simulations is 2.5 fs. The liquid sample is first annealed at 1600 K for 1 ns to reach equilibrium and then cooled down to 300 K at 10^{12} and 10^{13} K/s for the two compositions. In addition, MD simulations at 800 K (just above the glass-transition temperature as can be seen later in Fig. 10) are performed to investigate the SLI profiles and migration where initially one part of the simulation cell contains the crystal seeds (Pd_3Si or Pd_9Si_2) and the other part contains the corresponding liquid with the same composition. In these MD simulations, there are 2048 and 2376 atoms in the cell at the Pd_3Si and Pd_9Si_2 composition, respectively. The x direction which is perpendicular to the SLI is allowed to change and the $NP\gamma T$ ensemble is employed using the Nosé-Hoover thermostat under periodic boundary conditions. The time step is 3 fs and the total simulation time is 12 ns at each composition.

D. Crystal-structure search using genetic algorithm

Genetic algorithm (GA) code is linked to the DEEPMMD-KIT package and then the generated NNP is used to perform crystal-structure prediction for Pd-Si system. For the purpose of comparison, GA crystal-structure prediction is also performed with the EAM potential from the literature for Pd-Si system [37]. The crystal unit cells containing 16 atoms for Pd_3Si and 44 atoms for Pd_9Si_2 are used in the GA search. In addition, the GA search is performed five times at each composition with the initial structures belonging to random symmetry groups to improve statistics. The pool size for the GA search is 400 and the search is considered to be converged when the lowest energy of all the structures remains unchanged in 500 consecutive GA generations.

III. RESULTS AND DISCUSSION

A. Performance of the NNP for liquid structures

The performance of the NNP (Supplemental Material [53]) for liquid structures of $\text{Pd}_{82}\text{Si}_{12}$ and $\text{Pd}_{75}\text{Si}_{25}$ in the training and validating datasets are shown in Figs. 1 and 2,

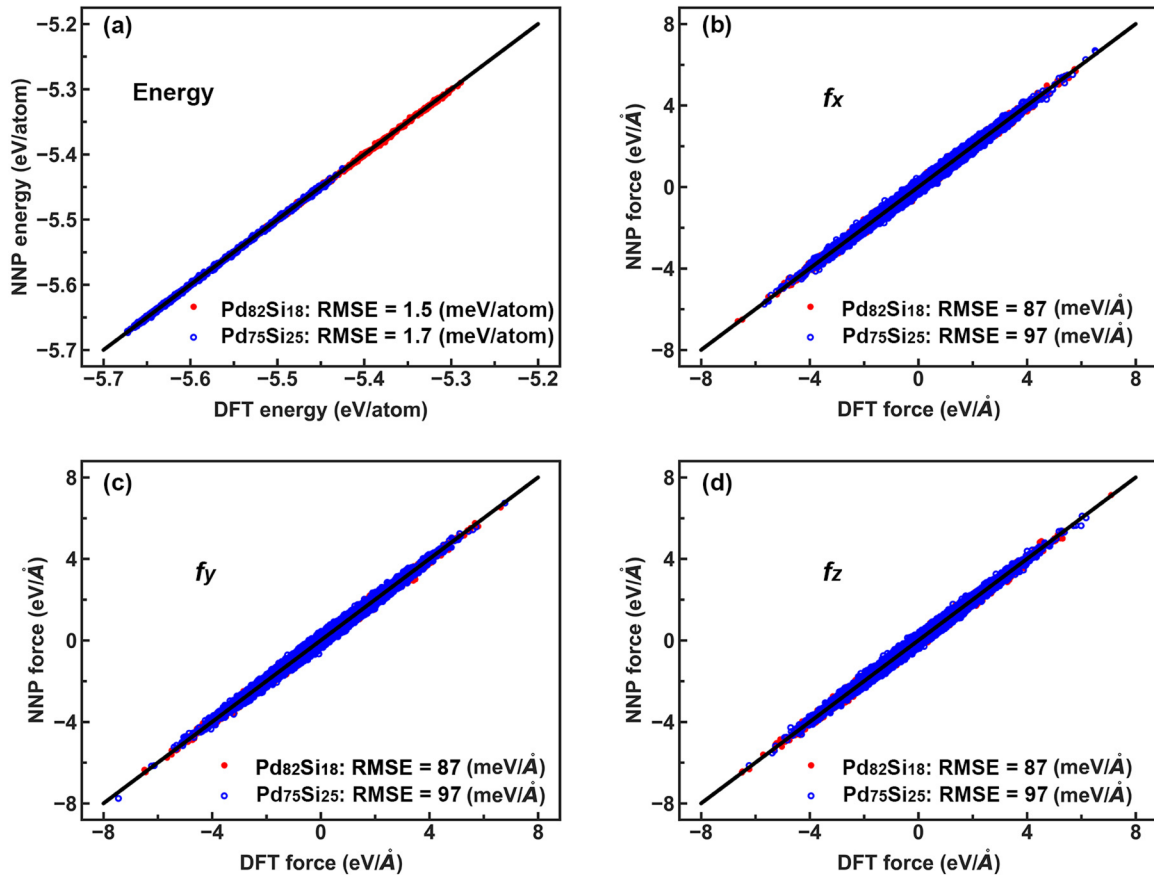


FIG. 1. NNP vs DFT energies and forces for Pd₈₂Si₁₈ and Pd₇₅Si₂₅ liquid structures in the training data. The corresponding RMSEs are shown for each system.

respectively. The root-mean-square errors (RMSEs) for the NNP energies and forces from the structures in the training set in comparison with those from static calculations on AIMD structures are less than 1.7 meV/atom for the energies and 100 meV/Å for the forces, while the RMSE for the structures in the validating set is less than 1.5 meV/atom for the energies and 95 meV/Å for the forces. We can see that the RMSEs from the training and validating sets are comparable to each other. These results indicate that overfitting in ML is unlikely to occur in this case and the information learned at higher temperatures can indeed predict the atomic motion at lower temperatures. The energy RMSE of less than 2.0 meV/atom and the force RMSE of less than 100 meV/Å are acceptable and the generated NNP should be promising to describe the liquid structures accurately.

Figure 3 displays the comparison of the PDFs for the liquids of Pd₈₂Si₁₈ and Pd₇₅Si₂₅ at 1600 K obtained by AIMD, NNP, and the EAM potential, respectively. It can be found that the PDFs from the NNP are in a very good agreement with that from AIMD up to the distance of 10 Å indicating that the NNP can also accurately describe the longer-range atomic correlations. However, the results from the EAM potential underestimate the interaction among the Pd atoms and overestimate the bonding between the Pd and Si atoms, as can be seen in Figs. 3(b) and 3(c) and Figs. 3(f) and 3(g), where the EAM potential gives the weakest first peak in the Pd-Pd partial PDF and strongest first peak in the

Pd-Si partial PDF. In addition, the Si-Si partial PDF from the EAM potential deviates much from that by AIMD and a small prepeak around 2.3 Å in Si-Si partial PDF shown in Figs. 3(d) and 3(h) obtained by the EAM potential is not seen in either AIMD or NNP-MD simulations.

We also investigate how NNP captures the atomic-level short-range order (SRO) motifs in the liquids as compared with the results from AIMD and the EAM potential simulations. We perform cluster-template alignment [38,39] to quantify the degree of the SRO in the liquids. Common motifs like bcc, fcc, hcp, and ICO as well as the recently excavated Pd-centered 1551 (Z13) and Si-centered Z9 motifs [52] are used as templates in our cluster-template alignment. The alignment score of 0.15 is used as the cutoff to assign the SRO motif to the Pd-centered or Si-centered clusters. If a cluster has an alignment score less than 0.15 for more than one template, the lowest alignment score is used to assign the cluster to the corresponding motif. It should be noted that the same cutoff value has been used in other systems to identify the SRO, such as Ni-Zr and Ni-Nb systems [50,51] and the relative ratios between different motifs are not dependent on the choice of the cutoff value as long as this value is reasonable. The most dominant motifs for the liquid structures of Pd₈₂Si₁₈ and Pd₇₅Si₂₅ are the Pd-centered 1551 and Si-centered Z9 motifs, and the fractions of these dominant motifs as the function of temperature are plotted in Fig. 4. In general, the fractions of the dominant motifs in both Pd₈₂Si₁₈ and Pd₇₅Si₂₅ liquids

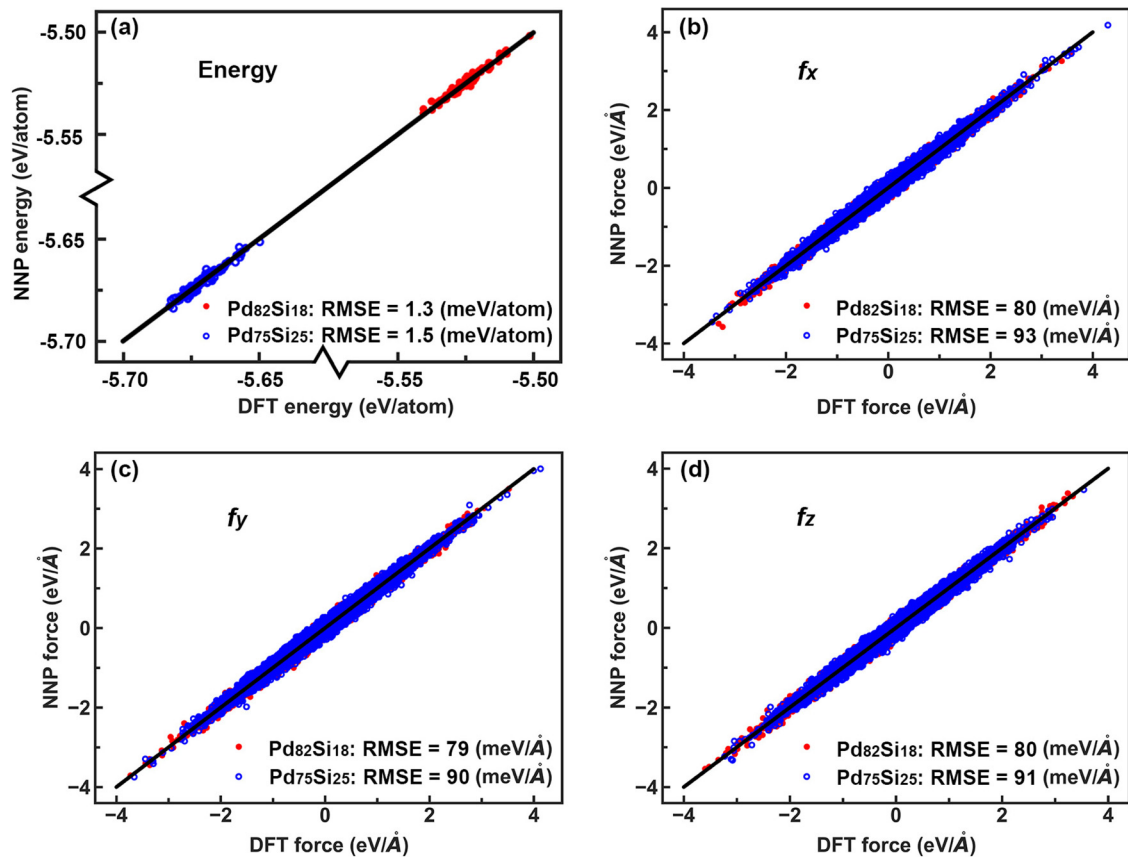


FIG. 2. NNP vs DFT energies and forces for $\text{Pd}_{82}\text{Si}_{18}$ and $\text{Pd}_{75}\text{Si}_{25}$ liquid structures in the validating data. The corresponding RMSEs are shown for each system.

increase as the temperature decreases from 1600 to 800 K, as one can see from Figs. 4(a)–4(d). The results from the NNP are in a much better agreement with the AIMD results, while the EAM potential underestimates the fractions of the SRO in both systems. Therefore, the generated NNP could depict the atomic interactions in the liquid more accurately than the EAM potential.

We note that for the Pd-centered clusters in both systems, the fraction of the dominant SRO, namely 1551 motif, is still less than 5% with respect to the total Pd-centered clusters at 800 K indicating that the first shell of Pd atom is considerably disordered. However, for the Si-centered clusters in both systems, the fraction of the Z9 motif is larger than 15% with respect to the total Si-centered clusters at 800 K from AIMD

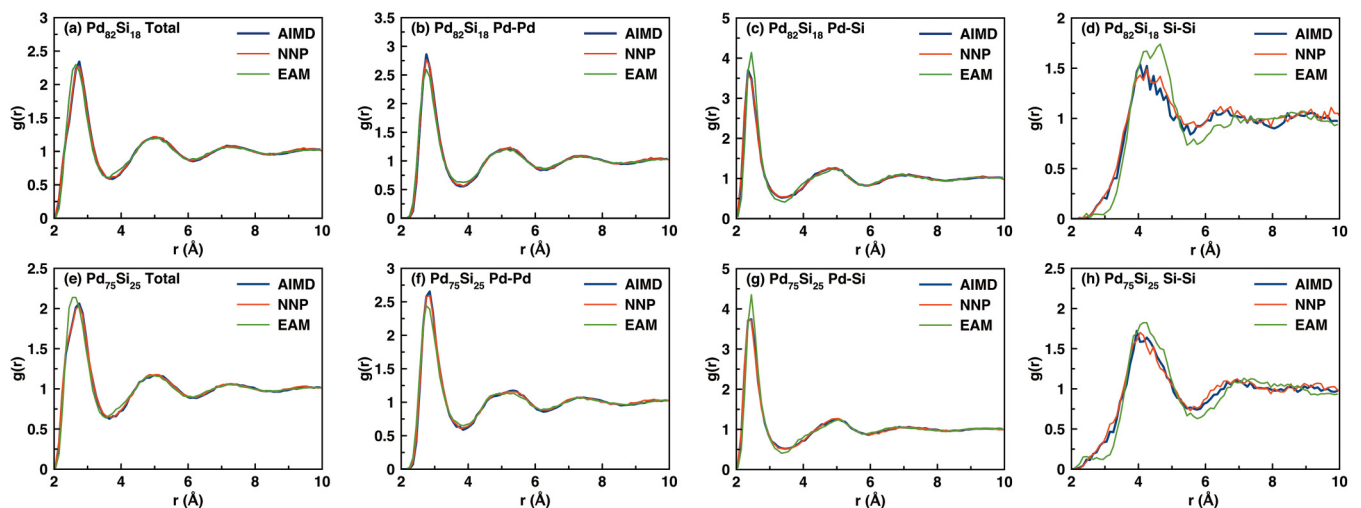


FIG. 3. Comparison of the pair distribution functions of (a)–(d) $\text{Pd}_{82}\text{Si}_{18}$ and (e)–(h) $\text{Pd}_{75}\text{Si}_{25}$ at 1600 K obtained by AIMD (blue), NNP (red), and the EAM potential (green).

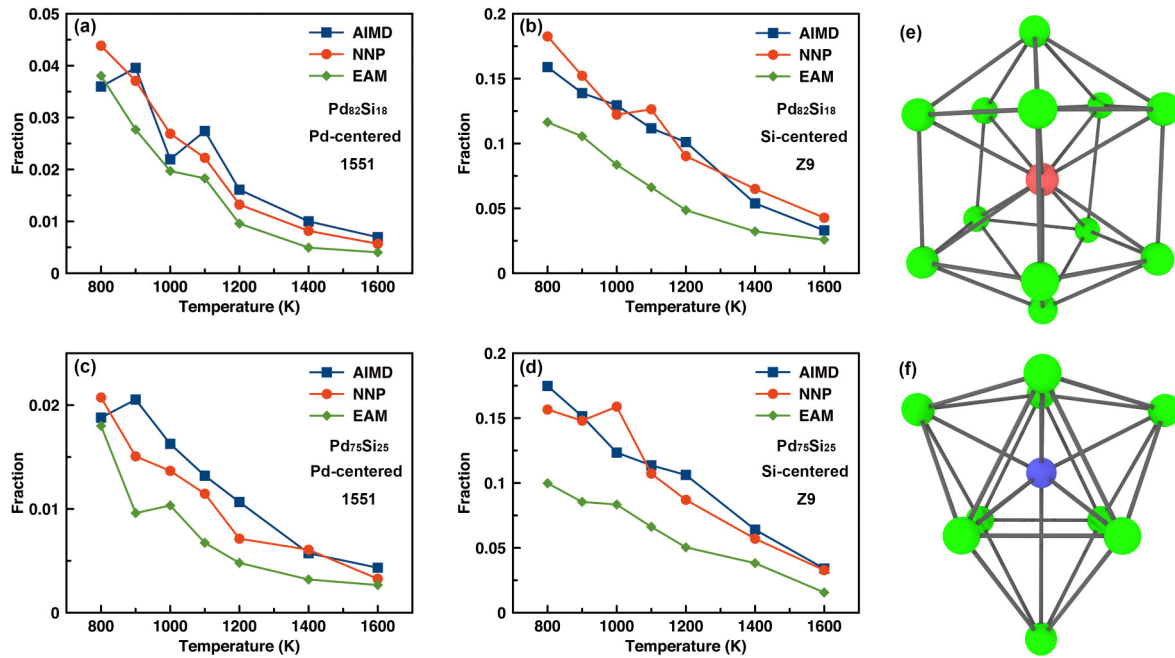


FIG. 4. Fractions of the dominant motifs for Pd-centered (a), (c) and Si-centered (b), (d) clusters in the structures for both systems at different temperatures. (e) shows the Pd-centered 1551 template and (f) exhibits the Si-centered Z9 template.

or the NNP. It should be noted that the Si-centered Z9 cluster is often referred to as a trigonal prism capped with three half octahedra [46,52], which is a “crystal gene” in Pd_3Si crystalline phase.

B. Performance of the NNP for crystal structures

Figures 5 and 6 show the RMSEs in the energies and forces for the undistorted and distorted crystal structures of Pd_3Si and Pd_9Si_2 compositions in the training set and validating set, respectively (see Computational Methods above) when comparing the NNP results with respect to the DFT results. The RMSEs are still small at these two compositions with less than 3 meV/atom for the energies and less than 90 meV/Å for the forces in the training and validating data. Comparing the results between two compositions, the energy errors at Pd_3Si are larger than that at Pd_9Si_2 , while the force errors are on the contrary. For the AIMD structures at 300 K, the RMSEs between the NNP and DFT are 1.4 meV/atom and 51 meV/Å for Pd_3Si and 0.7 meV/atom and 56 meV/Å for Pd_9Si_2 , respectively. In addition, the comparison of the PDFs for the solid phases of Pd_3Si and Pd_9Si_2 at 300 K obtained by AIMD and NNP is displayed in Fig. 7. It can be found that the PDFs from NNP are in a good agreement with that from AIMD indicating that the NNP can well capture the MD process of Pd_3Si and Pd_9Si_2 crystalline phases at 300 K. In combination of the RMSEs and PDF comparisons between NNP and AIMD at 300 K, the generated NNP can perform well at room temperature (300 K).

To further validate that NNP is able to distinguish structures with different energies, we apply the potential to reconstruct the energy vs volume (E-V) curve implicitly contained in the datasets and the results are exhibited in Fig. 8. In the datasets (1000 structures) at each composition, there are 500

structures at the equilibrium volume (relative volume = 1) of the corresponding crystal structure including the perfect crystal structure and the randomly distorted structures as well as 500 randomly distorted structures at other volumes. From Fig. 8, it can be clearly seen that the NNP could reproduce the E-V curve in the datasets very accurately and the energy of the perfect crystal phase is considerably lower than others.

The accurate description of the energies and forces by the NNP at these two compositions endows its promising application in the crystal-structure prediction. To demonstrate this, we perform GA structure search using the developed NNP to determine the ground-state structures of Pd_3Si and Pd_9Si_2 phases. The atomic position of these two structures are known in the literature. In our NNP development, these two ground-state structures are intentionally excluded from the training dataset. Details of the GA search have been described in Sec. IID. For the purpose of comparison, GA searches for the low-energy structures of these two phases are also performed using the available EAM potential.

Figure 9 displays the lowest-energy structures discovered by the GA runs at the composition of Pd_3Si and Pd_9Si_2 by NNP [Figs. 9(a) and 9(b)] and the EAM potential [Figs. 9(c) and 9(d)]. The corresponding energies from DFT, NNP, and EAM calculations are also shown for comparison. For the GA searches at the composition of Pd_3Si , the ground-state structure of Pd_3Si crystal phase with the space group of 62 as shown in Fig. 9(a) can be found by NNP within a few generations in every one of the five GA runs. The discrepancy between the NNP and DFT energies for this structure is around 2 meV/atom. In contrast, all the five GA runs by the EAM potential for Pd_3Si discover a structure with the space group of 82 as shown in Fig. 9(c), whose energy by the EAM potential is 40 meV/atom lower than that of the known ground-state Pd_3Si crystal structure. When we calculate the

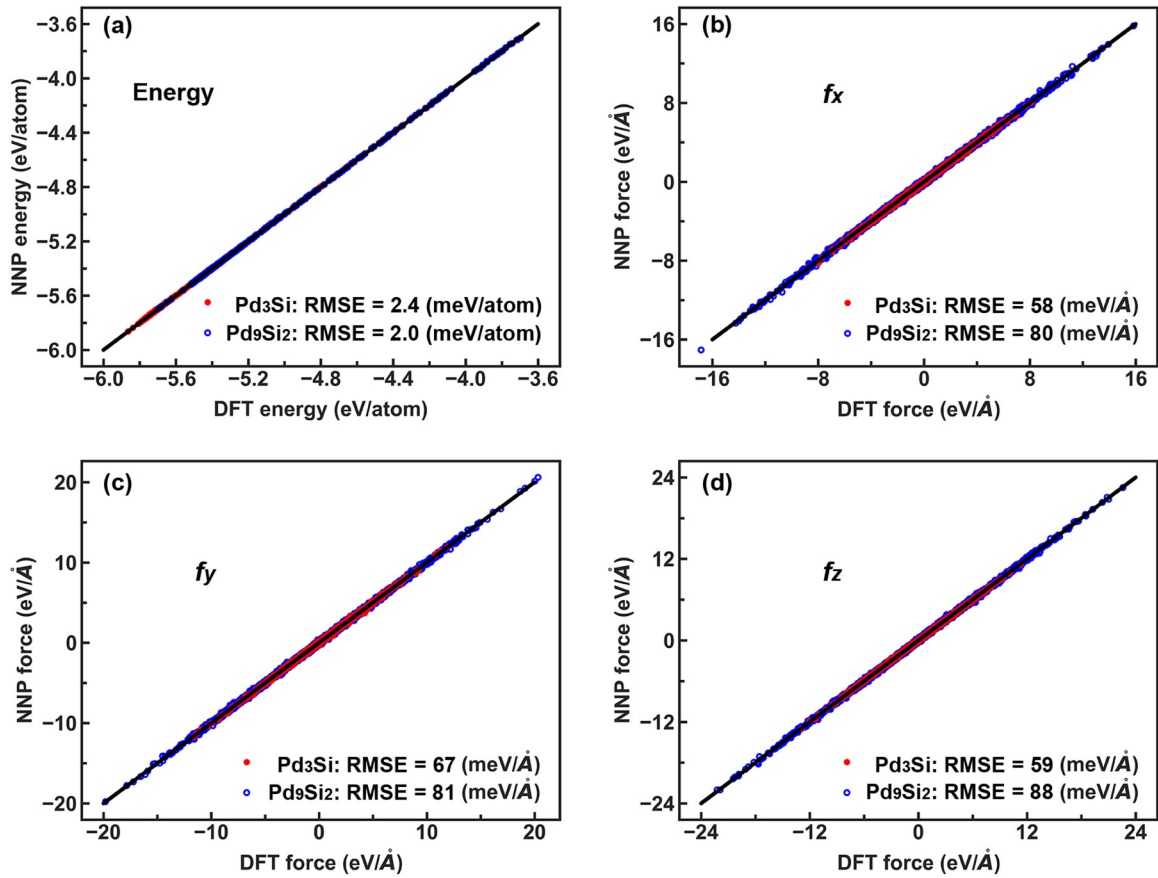


FIG. 5. NNP vs DFT energies and forces for Pd₃Si and Pd₉Si₂ crystal structures in the training data. The corresponding RMSEs are shown for each system.

energy of this structure by DFT and NNP, the energy is 33 and 28 meV/atom, respectively, higher than the known ground-state Pd₃Si crystal structure. These results indicate that the EAM potential fails to describe the energy ordering of crystal structures at the Pd₃Si composition. For the GA search at the Pd₉Si₂ composition with 44 atoms, the NNP also correctly captures the known ground-state structure as shown in Fig. 9(b) in every one of the five GA runs. The discrepancy in the energy for this structure by the NNP and DFT is only about 1 meV/atom, which indicates that the NNP potential is accurate in describing the energy landscape of different crystal structures. On the other hand, the GA search using the EAM potential fails to predict the ground-state structure of Pd₉Si₂. The lowest-energy structure obtained by the GA search using the EAM potential is shown in Fig. 9(d), which exhibits space group 1 symmetry and has energy 21 meV/atom lower than that of the ground-state structure shown in Fig. 9(b) by the EAM potential. We note that the failure in correctly predicting the ground-state structure of the Pd₉Si₂ phase is not the problem of the GA search (since it can get the lower-energy structure by the potential) but the accuracy problem of the EAM potential. Indeed, DFT and NNP calculations show that the lowest-energy structure of Pd₉Si₂ predicted by the EAM potential shown in Fig. 9(d) has energy of 29 and 35 meV/atom, respectively, higher than that of the true ground-state structure shown in Fig. 9(b).

C. Performance of the NNP for glass-transition process and SLI

After demonstrating the performance of the NNP for the liquids and crystals, it is interesting to investigate the glass-transition process and SLI by MD simulations using the NNP. Figures 10(a) and 10(b) display the relationship between instantaneous potential energy ($E - 3k_B T$) [52,54,55] and temperature for Pd₇₅Si₂₅ and Pd₈₂Si₁₈, respectively, at the cooling rate of 10^{12} and 10^{13} K/s. It can be found that the glass-transition temperature (T_g) of Pd₇₅Si₂₅ and Pd₈₂Si₁₈ is similar to each other and a glassy sample with the lower energy can be obtained at the lower cooling rate. The T_g of Pd₈₂Si₁₈ at such a fast cooling rate is a little higher than that from experiment (645 K) which is measured at much lower cooling rate (1800 K/s) [56]. These results indicate that the generated NNP can reasonably well describe the glass-formation process for Pd₇₅Si₂₅ and Pd₈₂Si₁₈ considering that the higher cooling rate will result in the higher T_g [57]. In the MD simulation of SLI, 2048 atoms are used at the composition of Pd₃Si. Among them 1024 atoms are initially arranged in crystal structure and the other 1024 atoms are initially in liquid state so that a SLI parallel to the (100) plane of the Pd₃Si crystal is formed as shown in Fig. 10(c). The simulations are performed at 800 K with periodic boundary condition in all three directions. The change in the total energy (kinetic plus potential energy) with annealing time is displayed in Fig. 10(d). It can be seen that the total energy

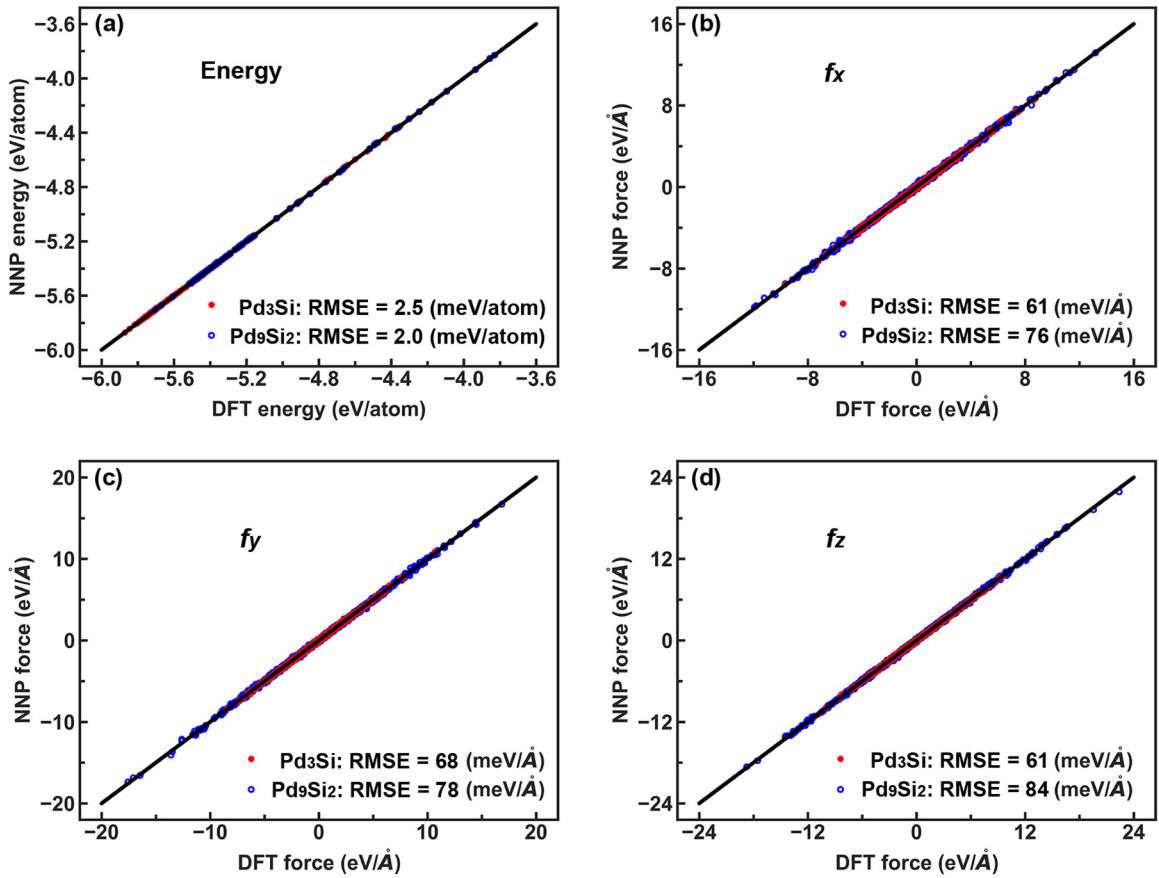


FIG. 6. NNP vs DFT energies and forces for Pd_3Si and Pd_9Si_2 crystal structures in the validating data. The corresponding RMSEs are shown for each system.

decreases continuously with the annealing time indicating that the crystalline phase continues to grow out of the liquid phase at 800 K. This crystallization process can be seen more clearly from Fig. 10(c) where almost the whole MD cell has been turned into the Pd_3Si crystalline phase at the MD simulation time of 12 ns. These results indicate that the liquidus temperature (T_l) at the composition of Pd_3Si by the

NNP should be above 800 K, which is consistent with the experimental observation and phase diagram [36]. The setup and MD simulation of SLI for the Pd_9Si_2 are carried out in the way similar to the case of Pd_3Si described above. The MD simulation cell contains 2376 atoms and initially 1188 atoms are arranged in the crystalline phase and the rest 1188 atoms are in the liquid phase as shown in Fig. 10(e). The

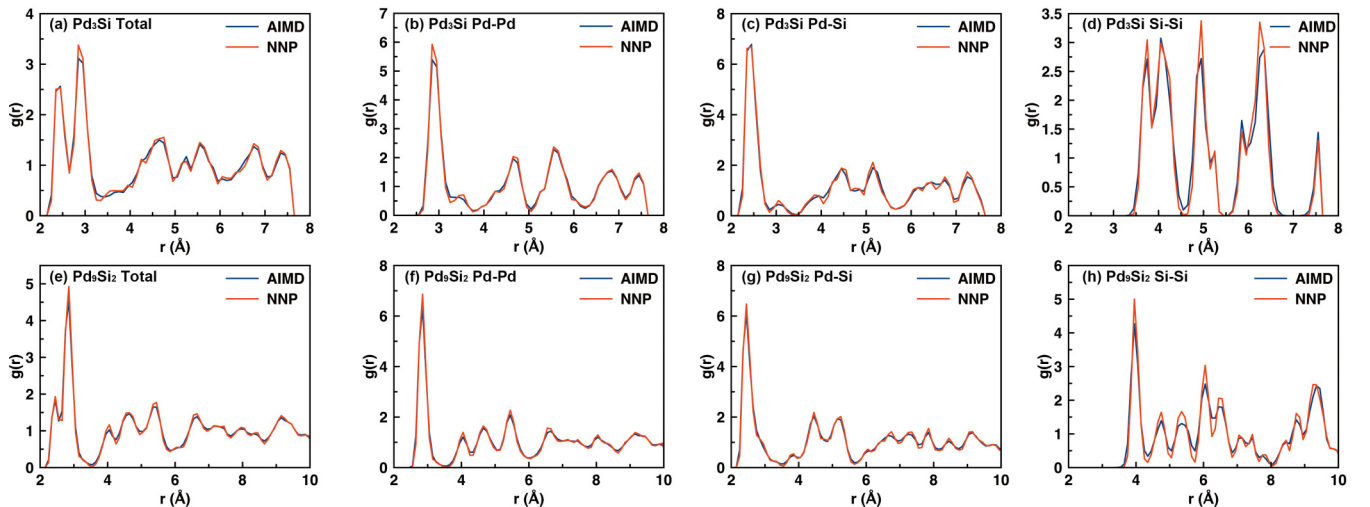


FIG. 7. Comparison of the pair distribution functions of (a)–(d) Pd_3Si and (e)–(h) Pd_9Si_2 at 300 K obtained by AIMD (blue) and NNP (red).

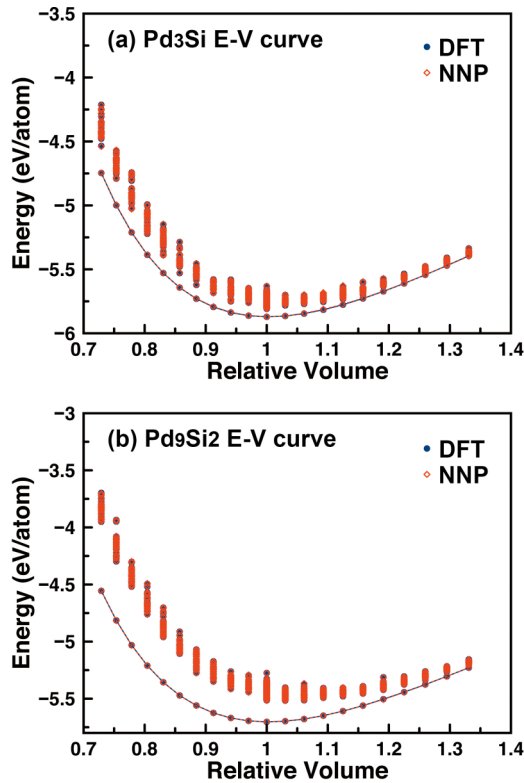


FIG. 8. E-V curve obtained by NNP and DFT calculations at the composition of (a) Pd_3Si and (b) Pd_9Si_2 . The relative volume denotes the ratio of the volume of crystal structure to that of the ground-state (a) Pd_3Si and (b) Pd_9Si_2 crystal structures, respectively. The results from NNP are almost identical to DFT, so they overlap with each other.

interface is parallel to the (100) plane of the Pd_9Si_2 crystal. In contrast to the case of Pd_3Si , the energy of the system decreases very slowly over the simulation time of 12 ns as shown in Fig. 10(f). The energy drop over the 12 ns is less than 0.03 eV/atom. A snapshot of the atomic structure at 12 ns as displayed in Fig. 10(e) shows that the Pd_9Si_2 crystal solidifies more slowly than Pd_3Si crystal at 800 K. These results suggest

that the crystallization kinetics for Pd_9Si_2 is slower than that for Pd_3Si at 800 K, which may be due to the relatively lower T_l of Pd_9Si_2 . This result is consistent with the phase diagram [36] that the T_l of Pd_9Si_2 is lower than that of Pd_3Si by more than 200 K and Pd_9Si_2 is around the eutectic composition. By comparing the T_g , T_l , and SLI profiles at Pd_3Si and Pd_9Si_2 , the value of T_g/T_l should be larger for Pd_9Si_2 than Pd_3Si , which indicates that the glass-forming ability (GFA) of $\text{Pd}_{82}\text{Si}_{18}$ should be better than Pd_3Si according to Turnbull [58]. In addition, the $\text{Pd}_{82}\text{Si}_{18}$ is around the eutectic composition and the eutectic instability could also trigger the "eutectic-glass" transition [59,60]. What is more, the critical cooling rate (R_c) is a frequently used criterion to denote the GFA of a system in experiment and the lower R_c suggests the better GFA. In this case, the R_c of $\text{Pd}_{82}\text{Si}_{18}$ is around 1800 K/s [56,61] while that of $\text{Pd}_{75}\text{Si}_{25}$ is around 10^6 K/s [61], which is consistent with the conclusion above that the GFA of $\text{Pd}_{82}\text{Si}_{18}$ should be better than Pd_3Si .

IV. SUMMARY

In the present work, the DEEPM scheme is applied to develop a machine learning neural-network interatomic potential for Pd-Si system containing complex mixed covalent and metallic bonding interactions. The developed NNP can accurately describe the energies and forces in comparison with the results from first-principles DFT calculations around the compositions of $\text{Pd}_{82}\text{Si}_{18}$ and $\text{Pd}_{75}\text{Si}_{25}$ with the RMSEs on the training and validating datasets less than 3 meV/atom for the energies and 100 meV/Å for the forces for both the liquid and crystalline structures. We also show that the NNP yield more accurate description of the liquid structures than the existing EAM potential in comparison with the AIMD results. Moreover, the developed NNP describes well the energy landscape of various crystalline structures while the EAM potential fails to correctly predict the ground-state structure for the Pd_3Si and Pd_9Si_2 crystalline phases. MD simulations of glass-transition process, SLI, and crystal growth with thousands of atoms also indicate that the developed NNP can correctly capture the crystallization kinetics and GFA for these systems. We anticipate that the developed NNP can find promising applications in investigating and unveiling the atomic-level structures and dynamics of glass formation, nucleation, and crystallization in these systems. In addition, the developed NNP can also be used to explore complex metastable structures in these systems by combining it with genetic algorithm and first-principles calculations.

ACKNOWLEDGMENTS

We thank Dr. Xin Zhao for his help and guidance in crystal structure prediction using genetic algorithm. N.W. acknowledges the financial support from the National Natural Science Foundation of China (Grants No. 51671160 and No. 51271149). T.Q.W. was also partially supported by the National Natural Science Foundation of China under the above grant numbers. Work at Ames Laboratory was supported by the U.S. Department of Energy, Office of Science, Basic Energy Sciences, Division of Materials Science and Engineering, including the computer time support on National

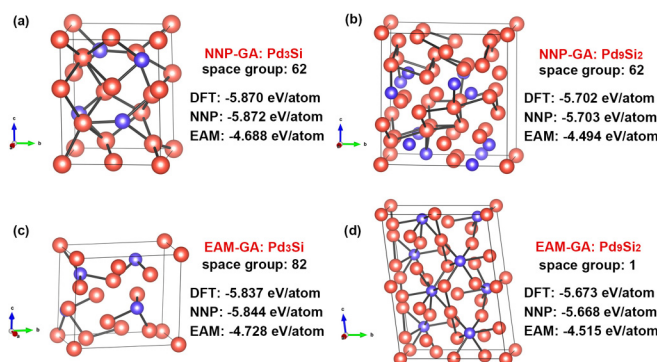


FIG. 9. Lowest-energy structures obtained from the classical GA searches at the composition of Pd_3Si and Pd_9Si_2 by NNP (a), (b) and EAM (c), (d) with the corresponding DFT, NNP, and EAM energies. The red and blue balls stand for Pd and Si atoms, respectively and the bonds are plotted for connecting the nearest neighbors.

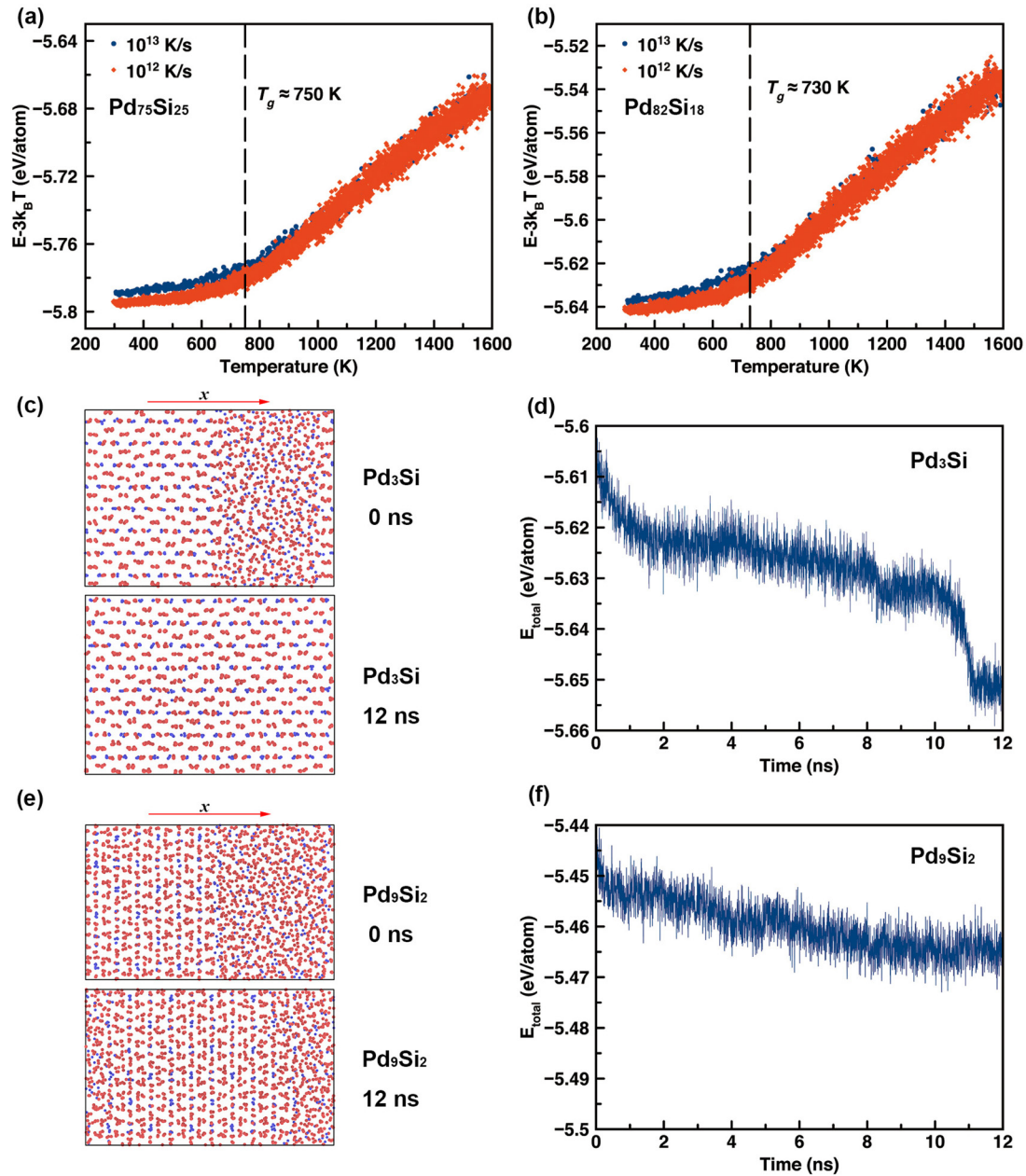


FIG. 10. (a) and (b) display the instantaneous energy ($E - 3k_B T$) as a function of temperature at different cooling rates for $\text{Pd}_{75}\text{Si}_{25}$ and $\text{Pd}_{82}\text{Si}_{18}$, respectively. (c) and (e) exhibit the snapshots at different annealing times of the composition at Pd_3Si and Pd_9Si_2 , respectively. The red balls denote the Pd atoms and the blue ones represent the Si atoms. (d) and (f) show the change in the total energy during the annealing process of the Pd_3Si and Pd_9Si_2 compositions, respectively, at 800 K obtained by NNP.

Energy Research Scientific Computing Center (NERSC) in Berkeley, CA. Ames Laboratory is operated for the U.S.

DOE by Iowa State University under Contract No. DE-AC02-07CH11358.

- [1] D. Frenkel and B. Smit, *Understanding Molecular Simulation: From Algorithms to Applications*, 2nd ed. (Academic, San Diego, 2002).
- [2] D. C. Rapaport, *The Art of Molecular Dynamics Simulation*, 2nd ed. (Cambridge University Press, Cambridge, England, 2004).
- [3] G. Kresse and J. Hafner, Ab initio molecular dynamics for liquid metals, *Phys. Rev. B* **47**, 558 (1993).
- [4] R. Car and M. Parrinello, Unified Approach for Molecular Dynamics and Density-Functional Theory, *Phys. Rev. Lett.* **55**, 2471 (1985).
- [5] L. Verlet, Computer “experiments” on classical fluids. I. Thermodynamical properties of Lennard-Jones molecules, *Phys. Rev.* **159**, 98 (1967).
- [6] R. W. Zwanzig, High-temperature equation of state by a perturbation method. I. Nonpolar gases, *J. Chem. Phys.* **22**, 1420 (1954).

- [7] J. Tersoff, Modeling solid-state chemistry: Interatomic potentials for multicomponent systems, *Phys. Rev. B* **39**, 5566 (1989).
- [8] R. L. C. Vink, G. T. Barkema, W. F. van der Weg, and N. Mousseau, Fitting the Stillinger–Weber potential to amorphous silicon, *J. Non-Cryst. Solids* **282**, 248 (2001).
- [9] M. S. Daw and M. I. Baskes, Embedded-atom method: Derivation and application to impurities, surfaces, and other defects in metals, *Phys. Rev. B* **29**, 6443 (1984).
- [10] H. W. Sheng, E. Ma, and M. J. Kramer, Relating dynamic properties to atomic structure in metallic glasses, *JOM* **64**, 856 (2012).
- [11] Y. Q. Cheng and E. Ma, Atomic-level structure and structure–property relationship in metallic glasses, *Prog. Mater. Sci.* **56**, 379 (2011).
- [12] D. J. Hepburn and G. J. Ackland, Metallic-covalent interatomic potential for carbon in iron, *Phys. Rev. B* **78**, 165115 (2008).
- [13] C. M. Bishop, *Pattern Recognition and Machine Learning* (Springer, New York, 2006).
- [14] J. Behler and M. Parrinello, Generalized Neural-Network Representation of High-Dimensional Potential-Energy Surfaces, *Phys. Rev. Lett.* **98**, 146401 (2007).
- [15] R. Z. Khaliullin, H. Eshet, T. D. Kühne, J. Behler, and M. Parrinello, Nucleation mechanism for the direct graphite-to-diamond phase transition, *Nat. Mater.* **10**, 693 (2011).
- [16] N. Artrith and A. Urban, An implementation of artificial neural-network potentials for atomistic materials simulations: Performance for TiO₂, *Comput. Mater. Sci.* **114**, 135 (2016).
- [17] S. Faraji, S. A. Ghasemi, S. Rostami, R. Rasoulkhani, B. Schaefer, S. Goedecker, and M. Amsler, High accuracy and transferability of a neural network potential through charge equilibration for calcium fluoride, *Phys. Rev. B* **95**, 104105 (2017).
- [18] L. Zhang, J. Han, H. Wang, R. Car, and W. E, Deep Potential Molecular Dynamics: A Scalable Model with the Accuracy of Quantum Mechanics, *Phys. Rev. Lett.* **120**, 143001 (2018).
- [19] L. Zhang, J. Han, H. Wang, W. A. Saidi, R. Car, and W. E, in *Advances in Neural Information Processing Systems*, edited by S. Bengio, H. Wallach, H. Larochelle, K. Grauman, N. Cesa-Bianchi, and R. Garnett (Curran Associates, Inc., 2018), Vol. 31, pp. 4441–4451.
- [20] L. Zhang, D. Y. Lin, H. Wang, R. Car, and W. E, Active learning of uniformly accurate interatomic potentials for materials simulation, *Phys. Rev. Mater.* **3**, 023804 (2019).
- [21] H. Wang, L. Zhang, J. Han, and W. E, DeePMD-kit: A deep learning package for many-body potential energy representation and molecular dynamics, *Comput. Phys. Commun.* **228**, 178 (2018).
- [22] K. T. Schütt, H. E. Sauceda, P.-J. Kindermans, A. Tkatchenko, and K.-R. Müller, SchNet - A deep learning architecture for molecules and materials, *J. Chem. Phys.* **148**, 241722 (2018).
- [23] K. T. Schütt, P. Kessel, M. Gastegger, K. A. Nicoli, A. Tkatchenko, and K.-R. Müller, SchNetPack: A deep learning toolbox for atomistic systems, *J. Chem. Theory Comput.* **15**, 448 (2019).
- [24] T. S. Hy, S. Trivedi, H. Pan, B. M. Anderson, and R. Kondor, Predicting molecular properties with covariant compositional networks, *J. Chem. Phys.* **148**, 241745 (2018).
- [25] A. P. Bartók, M. C. Payne, R. Kondor, and G. Csányi, Gaussian Approximation Potentials: The Accuracy of Quantum Mechanics, without the Electrons, *Phys. Rev. Lett.* **104**, 136403 (2010).
- [26] D. Dragoni, T. D. Daff, G. Csányi, and N. Marzari, Achieving DFT accuracy with a machine-learning interatomic potential: Thermomechanics and defects in bcc ferromagnetic iron, *Phys. Rev. Mater.* **2**, 013808 (2018).
- [27] A. P. Bartók, J. Kermode, N. Bernstein, and G. Csányi, Machine Learning a General-Purpose Interatomic Potential for Silicon, *Phys. Rev. X* **8**, 041048 (2018).
- [28] C. Chen, Z. Deng, R. Tran, H. Tang, I. -H. Chu, and S. P. Ong, Accurate force field for molybdenum by machine learning large materials data, *Phys. Rev. Mater.* **1**, 043603 (2017).
- [29] X.-G. Li, C. Hu, C. Chen, Z. Deng, J. Luo, and S. P. Ong, Quantum-accurate spectral neighbor analysis potential models for Ni-Mo binary alloys and fcc metals, *Phys. Rev. B* **98**, 094104 (2018).
- [30] Z. Deng, C. Chen, X. -G. Li, and S. P. Ong, An electrostatic spectral neighbor analysis potential for lithium nitride, *npj Comput. Mater.* **5**, 75 (2019).
- [31] A. V. Shapeev, Moment tensor potentials: A class of systematically improvable interatomic potentials, *Multiscale Model. Simul.* **14**, 1153 (2016).
- [32] E. V. Podryabinkin and A. V. Shapeev, Active learning of linearly parametrized interatomic potentials, *Comput. Mater. Sci.* **140**, 171 (2017).
- [33] K. Gubaev, E. V. Podryabinkin, G. L. W. Hart, and A. V. Shapeev, Accelerating high-throughput searches for new alloys with active learning of interatomic potentials, *Comput. Mater. Sci.* **156**, 148 (2019).
- [34] Y. Zuo, C. Chen, X. Li, Z. Deng, Y. Chen, J. Behler, G. Csányi, A. V. Shapeev, A. P. Thompson, M. A. Wood, and S. P. Ong, A performance and cost assessment of machine learning interatomic potentials, [arXiv:1906.08888](https://arxiv.org/abs/1906.08888).
- [35] K. F. Yao and N. Chen, Pd-Si binary bulk metallic glass, *Sci. China* **51**, 414 (2008).
- [36] N. Saunders, Phase diagram calculations for eight glass forming alloy systems, *Calphad* **9**, 297 (1985).
- [37] PdSi EAM potentials <https://sites.google.com/site/eampotentials/Home/PdSi>.
- [38] X. W. Fang, C. -Z. Wang, Y. X. Yao, Z. J. Ding, and K. -M. Ho, Atomistic cluster alignment method for local order mining in liquids and glasses, *Phys. Rev. B* **82**, 184204 (2010).
- [39] Y. Sun, F. Zhang, Z. Ye, Y. Zhang, X. Fang, Z. Ding, C.-Z. Wang, M. I. Mendelev, R. T. Ott, M. J. Kramer, and K.-M. Ho, “Crystal genes” in metallic liquids and glasses, *Sci. Rep.* **6**, 23734 (2016).
- [40] S. Q. Wu, M. Ji, C.-Z. Wang, M. C. Nguyen, X. Zhao, K. Umemoto, R. M. Wentzcovitch, and K.-M. Ho, An adaptive genetic algorithm for crystal structure prediction, *J. Phys.: Condens. Matter* **26**, 035402 (2014).
- [41] X. Zhao, M. C. Nguyen, W. Y. Zhang, C.-Z. Wang, M. J. Kramer, D. J. Sellmyer, X. Z. Li, F. Zhang, L. Q. Ke, V. P. Antropov, and K.-M. Ho, Exploring the Structural Complexity of Intermetallic Compounds by an Adaptive Genetic Algorithm, *Phys. Rev. Lett.* **112**, 045502 (2014).
- [42] G. Kresse and J. Furthmüller, Efficient iterative schemes for ab initio total-energy calculations using a plane-wave basis set, *Phys. Rev. B* **54**, 11169 (1996).

- [43] P. E. Bloch, Projector augmented-wave method, *Phys. Rev. B* **50**, 17953 (1994).
- [44] J. P. Perdew, K. Burke, and M. Ernzerhof, Generalized Gradient Approximation Made Simple, *Phys. Rev. Lett.* **77**, 3865 (1996).
- [45] M. Durandurdu, *Ab initio* modeling of metallic Pd₈₀Si₂₀ glass, *Comput. Mater. Sci.* **65**, 44 (2012).
- [46] F. Dong, G. Q. Yue, Y. R. Guo, C. Qiao, Z. Y. Wang, Y. X. Zheng, R. J. Zhang, Y. Sun, W. S. Su, M. J. Kramer, S. Y. Wang, C. Z. Wang, K. M. Ho, and L. Y. Chen, Si-centered capped trigonal prism ordering in liquid Pd₈₂Si₁₈ alloy study by first-principles calculations, *RSC Adv.* **7**, 18093 (2017).
- [47] D. Kingma and J. Ba, Adam: A method for stochastic optimization, [arXiv:1412.6980](https://arxiv.org/abs/1412.6980).
- [48] S. Plimton, Fast parallel algorithms for short-range molecular dynamics, *J. Comput. Phys.* **117**, 1 (1995).
- [49] Y. Sun, Y. Zhang, F. Zhang, Z. Ye, Z. Ding, C.-Z. Wang, and K.-M. Ho, Cooling rate dependence of structural order in Al₉₀Sm₁₀ metallic glass, *J. Appl. Phys.* **120**, 015901 (2016).
- [50] T. Q. Wen, L. Tang, Y. Sun, K.-M. Ho, C.-Z. Wang, and N. Wang, Crystal genes in a marginal glass-forming system of Ni₅₀Zr₅₀, *Phys. Chem. Chem. Phys.* **19**, 30429 (2017).
- [51] T. Q. Wen, Y. Sun, B. Ye, L. Tang, Z. Yang, K.-M. Ho, C.-Z. Wang, and N. Wang, Cooling rate dependence of structural order in Ni₆₂Nb₃₈ metallic glass, *J. Appl. Phys.* **123**, 045108 (2018).
- [52] Z. J. Yang, L. Tang, T. Q. Wen, K.-M. Ho, and C.-Z. Wang, Effects of Si solute on the glass formation and atomic structure of Pd liquid, *J. Phys.: Condens. Matter* **31**, 135701 (2019).
- [53] See Supplemental Material at <http://link.aps.org/supplemental/10.1103/PhysRevB.100.174101> for the developed neural-network potential for Pd-Si system.
- [54] L. Tang, T. Q. Wen, N. Wang, Y. Sun, F. Zhang, Z. J. Yang, K.-M. Ho, and C.-Z. Wang, Structural and chemical orders in Ni_{64.5}Zr_{35.5} metallic glass by molecular dynamics simulation, *Phys. Rev. Mater.* **2**, 033601 (2018).
- [55] M. I. Mendeleev, F. Zhang, Z. Ye, Y. Sun, M. C. Nguyen, S. R. Wilson, C.-Z. Wang, and K.-M. Ho, Development of interatomic potentials appropriate for simulation of devitrification of Al₉₀Sm₁₀ alloy, *Model. Simul. Mater. Sci. Eng.* **23**, 045013 (2015).
- [56] T. Q. Wen, W. J. Yao, and N. Wang, Correlation between the Arrhenius crossover and the glass forming ability in metallic glasses, *Sci. Rep.* **7**, 13164 (2017).
- [57] P. G. Debenedetti and F. H. Stillinger, Supercooled liquids and the glass transition, *Nature (London)* **410**, 259 (2001).
- [58] D. Turnbull, Under what conditions can a glass be formed? *Contemp. Phys.* **10**, 473 (1969).
- [59] N. Wang, L. Ji, W. J. Yao, and Y. P. Zheng, Correlation between fragility and eutectic instability and glass-forming ability in binary metallic glasses under growth controlled conditions, *J. Appl. Phys.* **111**, 103525 (2012).
- [60] N. Wang, Y. E. Kalay, and R. Trivedi, Eutectic-to-metallic glass transition in the Al-Sm system, *Acta Mater.* **59**, 6604 (2011).
- [61] Z. P. Lu, H. Bei, and C. T. Liu, Recent progress in quantifying glass-forming ability of bulk metallic glasses, *Intermetallics* **15**, 618 (2007).